Multiloop atom interferometer measurements of chameleon dark energy in microgravity

Sheng-wey Chiow and Nan Yu

Phys. Rev. D **97**, 044043 — Published 28 February 2018

DOI: 10.1103/PhysRevD.97.044043

Multi-loop atom interferometer measurements of chameleon dark energy in microgravity

Sheng-wey Chiow and Nan Yu*
Jet Propulsion Laboratory, California Institute of Technology, Pasadena, CA 91109
(Dated: February 6, 2018)

Chameleon field is one of the promising candidates of dark energy scalar fields. As in all viable candidate field theories, a screening mechanism is implemented to be consistent with all existing tests of general relativity. The screening effect in the chameleon theory manifests its influence limited only to the thin outer layer of a bulk object, thus producing extra forces orders of magnitude weaker than that of the gravitational force of the bulk. For point-like particles such as atoms, the depth of screening is larger than the size of the particle, such that the screening mechanism is ineffective and the chameleon force is fully expressed on the atomic test particles. Extra force measurements using atom interferometry are thus much more sensitive than bulk mass based measurements, and indeed have placed the most stringent constraints on the parameters characterizing chameleon field. In this paper, we present a conceptual measurement approach for chameleon force detection using atom interferometry in microgravity, in which multi-loop atom interferometers exploit specially designed periodic modulation of chameleon fields. We show that major systematics of the dark energy force measurements, i.e., effects of gravitational forces and their gradients, can be suppressed below all hypothetical chameleon signals in the parameter space of interest.

I. INTRODUCTION

The Universe is believed to be mostly composed of dark energy which is responsible for the observed accelerating expansion rate of the Universe [1]. While no one knows the exact nature of dark energy, it is assumed in the form of either cosmological constant or scalar fields. In the latter case, its interaction with normal matter should be of the strength of gravitational force. The lack of direct detection of the dark enery interaction, in the form of extra forces on test objects apart from the four known forces, leads to the necessity that any dark energy scalar field must be environmentally dependent and thus the influence of dark energy may be greatly suppressed near dense material, often referred to as the screening mechanism [2]. Parameters in such scalar field theories are in turn bounded by precise experiments on, e.g., the inverse-square law of gravity, parameters in the parameterized post Newtonian (PPN) metric, and the equivalence principle, as summarized in Ref. [3]. Emerging from quantum field theories, chameleon theories satisfy the above requirements using only few parameters [4, 5]. Unique to chameleon theories is that small test particles do not suffer from the screening effect, rendering the approach of atom interferometric detection very attractive in theory validation [5]. While experimental efforts of atomic validation reported to date indeed have already constrained the chameleon parameters beyond classical means by orders of magnitude [6–8], the validity of the chameleon theory is still an open question.

In this paper, we present a measurement concept of direct detection of chameleon forces using atom interferometers in microgravity, with a sensitivity sufficient to detect any predicted chameleon force or rule out the theory completely. In this concept, gravitational forces are engineered to balance out such that tailored atom interferometers with a slowly and linear motion of atoms in microgravity can measure the chameleon force without precise knowledge of gravity, in contrast to experiments such as Refs. [6–8] where the accuracy of Newtonian force measurements sets the ultimate sensitivity limit on chameleon force detections. The detection is thus a direct measurement of forces resulting from the governing equation of motion of the chameleon field, independent of the gravitational constant G or its variations.

The paper is organized as follows. Section II briefly introduces the chameleon fields, targeted parameter space to tackle, and foreseen detection obstacles. Section III describes a numerical approach for calculating chameleon fields for different configurations, providing first order estimates of anticipated chameleon forces. Section IV reviews the path integral approach for the atom interferometer phase calculation, which serves as the basis of sensitivity estimates for different chameleon forces. Sections V and VI discuss in detail on two special categories of chameleon field measurement configurations: spherical and periodic. In both cases, realistic numbers are provided using currently available cold atom experiment capabilities. Finally, our findings are summarized in Section VII.

II. DETECTION OF THE CHAMELEON SCALAR FIELD

We follow the method of describing chameleon fields as outlined in Ref. [4, 5]. Chameleon theories include a self-interacting potential $V(\phi)$ of a scalar field ϕ, and an interaction potential $V_{\rm int}(\phi, \rho)$ with matter density ρ. We consider, in this paper, the effective potential in the

* nan.yu@jpl.nasa.gov

simplest and the lowest order inverse power-law form [4, 5]

$$V_{\rm eff}(\phi) \equiv V(\phi) + V_{\rm int}(\phi, \rho) = \Lambda^4 \left(1 + \frac{\Lambda^n}{\phi^n}\right) + \frac{\phi}{M}\rho, \quad (1)$$

where Λ sets the strength of the self-interaction, n is a positive integer, and M describes the interaction with normal matter. The equation of motion, in the static case where ρ and ϕ are stationary, is

$$\nabla^2\phi = \frac{\partial V_{\rm eff}}{\partial \phi} = -n\frac{\Lambda^{n+4}}{\phi^{n+1}} + \beta\frac{\rho}{M_{\rm Pl}}, \quad (2)$$

where $\beta = M_{\rm Pl}/M$ and $M_{\rm Pl}$ is the reduced Planck mass. The acceleration on a test particle due to an established field profile ϕ can be obtained from the spatial derivative of $V_{\rm int}$ [4, 5]:

$$\vec{a} = -\frac{\beta}{M_{\rm Pl}}\vec{\nabla}\phi. \quad (3)$$

Far away from boundaries, ϕ approaches an equilibrium value $\phi_{\rm eq}$ that minimizes $V_{\rm eff}$

$$\left.\frac{\partial V_{\rm eff}}{\partial \phi}\right|_{\phi_{\rm eq}} = 0,$$
$$\phi_{\rm eq}(\rho) = \left(\frac{\beta}{n\Lambda^{n+4}}\frac{\rho}{M_{\rm Pl}}\right)^{-\frac{1}{n+1}}. \quad (4)$$

The distance for ϕ to reach $\phi_{\rm eq}$ is short for typical matter densities, such that the interior of a bulk experiences zero acceleration from the chameleon field (Eq. (3)). The bulk, as a whole, experiences negligible chameleon acceleration, which is known as screening [5]. The screening does not happen to gaseous atoms, due to the microscopic size and dilute density, which makes atoms a much more sensitive tool for chameleon detection. The concept of using atomic test particles for chameleon force detections has been proposed [5] and experimentally implemented [6–8], where acceleration of atoms is precisely measured in a quantum interferometric way (see Section IV).

Despite the success of more strigent constraints on the chameleon theory parameters (n, Λ, β) by atom interferometer measurements [8], major systematic effects need to be addressed before a complete conclusion for the chameleon theory can be reached. Being an extra force, chameleon forces can at best be detected at the precision of known forces. This is evident in Ref. [8], where the statistical uncertainty and the uncertainty of the gravitational force from the test object are comparable. Further improvement on constraining chameleon parameters will require better knowledge of the test object mass distribution. Eventually a more precise value of G is necessary. At present G is known at $\sim 10^{-5}$ [9], which limits the overall measurement precession at a similar level.

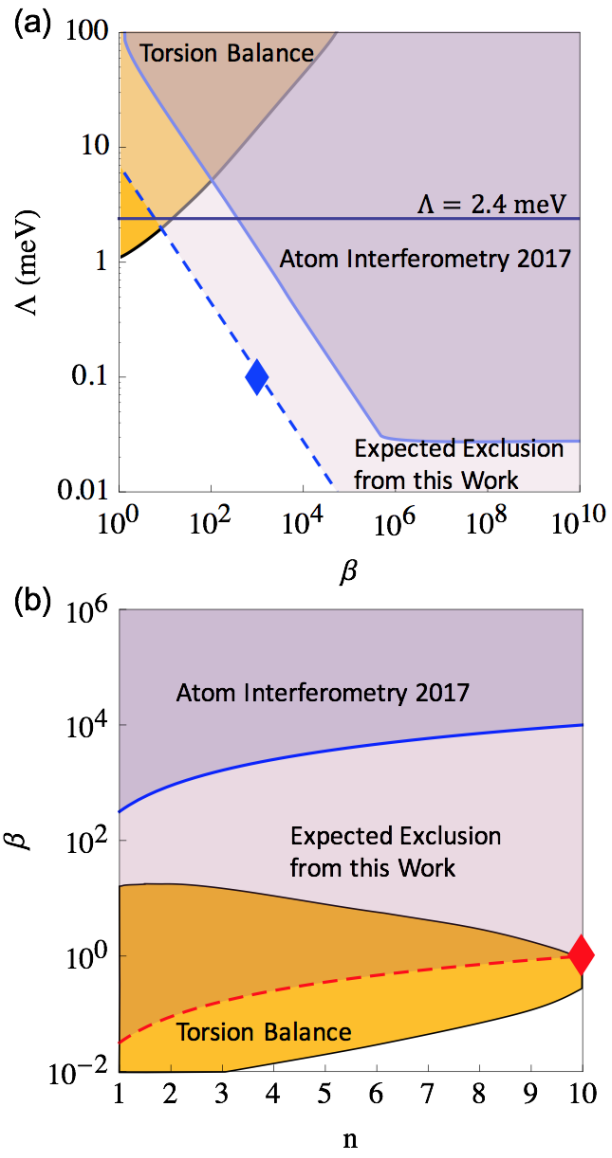

FIG. 1. Exclusion plots of chameleon parameters. (a) (β, Λ) exclusion plot for $n = 1$. Region near the upper left corner (yellow) is excluded by the torsion balance experiment [10]. Region bounded by the blue curve is excluded by the atom interferometer experiment in Ref. [8]. The blue diamond marks the parameter set of $(n, \Lambda, \beta) = (1, 0.1\ \text{meV}, 10^3)$, and the blue dashed line across it labels parameters that would produce the same chameleon force. Failure of detecting accelerations calculated in this work based on this parameter set will exclude the shaded region above the dashed line. $\Lambda = \Lambda_0$ is of cosmological relevance, and is shown as the horizontal line. (b) (n, β) exclusion plot for $\Lambda = \Lambda_0$. Regions excluded by the corresponding experiments are labelled. The red diamond marks the embracive parameter set of $(n, \Lambda, \beta) = (10, \Lambda_0, 1)$, and the red dashed curve across it labels parameters that would produce the same chameleon force. Failure of detecting accelerations calculated in this work based on this parameter set will exclude the shaded region above the dashed curve.

In order to estimate limitations and explore possibilities, we developed a numerical approach for calculating ϕ and thus $\vec{a}$ for various configurations, which facilitates the investigation for a class of practical measurement schemes that is immune to major systematics of chameleon force detection. Two parameter sets will be extensively discussed: $(n, \Lambda, \beta) = (1, 0.1 \text{ meV}, 10^3)$ and $(10, \Lambda_0 \simeq 2.4 \text{ meV}, 1)$. The former is in line with Ref. [7], which will exclude $n = 1$ chameleon theory completely if a null detection is concluded. Choosing the same parameters also allows direct comparison of results. The latter, referred to as the embracive parameter set, is the extreme point in the chameleon parameter space under the constraint of cosmological observation $\Lambda = \Lambda_0$. The exclusion of the embracive parameter set will invalidate the chameleon theory all together [8], which is the goal of the proposed experiment. Figure 1 summarizes current constraints on (n, Λ, β) and expected improvements if predicted accelerations calculated with the above parameter sets are not detected.

Note that due to the screening effect, the profile of the chameleon field inside an enclosed container is not affected by the external field distribution, while the same equation of motion of Eq. (2) applies everywhere. This feature grants the possibility of performing chameleon theory tests inside a vacuum chamber without worrying about mass distributions outside the vacuum chamber far away from the test masses under consideration [5–8]. They do introduce systematics due to gravity gradients.

III. NUMERICAL METHOD

Since atoms will be the test particles for chameleon force measurements under an ultra high vacuum (UHV) environment, we are interested in ϕ in a UHV region enclosed by a metal container. Due to the screening effect that ϕ approaches equilibrium ϕ_{eq} in short distances inside dense material, a metal container effectively separate ϕ inside the enclosed volume from the rest of the world. The task of solving ϕ for a certain vacuum chamber geometry is then reduced to solving the nonlinear partial differential equation (PDE) of Eq. (2) for given (n, Λ, β) and a position dependent density function $\rho = \rho_{\text{vacuum}}$ or ρ_{wall}. $rho_{\text{vacuum}} = 6.6 \times 10^{-17}$ g/cm^3 is the density in UHV, corresponding to a commonly available residual pressure of 6×10^{-10} Torr in a cold atom apparatus. $\rho_{\text{wall}} = 7$ g/cm^3 is the nominal density of steel that vacuum chambers are typically made of. The boundaries of the numerical calculation are located inside the walls of the vacuum chamber with boundary conditions for the PDE set as $\phi = \phi_{\text{eq}}(\rho_{\text{wall}})$.

We use a commercial numerical package with a partial differential equation toolbox on a laptop for solving Eq. (2), instead of resorting to customized implementation of numerical schemes or algorithms [7]. Solving a nonlinear PDE often requires a good initial guess solution for iterative refinements. In addition, the huge difference of ρ_{wall} and ρ_{vacuum} across material surfaces could make the solution highly unstable, and thus special cares might be needed. We find that it is not necessary to separate ϕ in different regions of ρ and then match ϕ at the interfaces. Equation (2) is solved on the whole domain with the PDE solver by first setting the initial guess to a constant value of $\phi_{\text{eq}}(\rho_{\text{wall}})$, and iteratively feeding the solution as the initial guess for the next run,. A satisfactory solution can be obtained after several iterations, and the iteration is stopped when the fractional change between successive solutions is smaller than a designated value. The capability to solve the whole system in one PDE setting allows arbitrarily shaped vacuum confinements, which will be greatly exploited in Section VI. Note that a satisfactory solution here refers to a solution that agrees with that obtained by other means, which will be clarified in the following sections.

IV. ATOM INTERFEROMETER COUPLING TO CHAMELEON FIELDS

Light pulse atom interferometry utilizes the wave nature of atoms for sensitive measurements, where the matter wave of each atom is split, reflected, and recombined to interfere by laser pulses [11–14]. The phase difference between wave packet paths, due to atomic motion, gravity, magnetic fields, etc., is measured against the phase of the laser pulses. The sensitivity of an atom interferometer (AI) increases as the pulse separation time T, the interrogation time of the AI. For experiments demanding high sensitivities, long T AIs are proposed [14, 15] and constructed [16–18] in both terrestrial and microgravity environments.

To distinguish systematics from desired signals, detailed analyses on AI phases are crucial for sensitive measurements [14, 15, 19, 20]. In this paper, we elect to calculate the AI phases in the nonrelativistic perturbative method summarized as follows. The phase ψ of an AI can be decomposed into three parts: the propagation phase ψ_{prop}, the laser phase ψ_{laser}, and the separation phase ψ_{separate} [14]. Consider an AI that each atom can take either trajectory 1 or trajectory 2 to move from the first beamsplitter to the last beamsplitter. The propagation phase of the AI is

$$\psi_{\text{prop}} = \frac{1}{\hbar}\left[\int_1 \left(\frac{m}{2}v^2 - V\right) dt - \int_2 \left(\frac{m}{2}v^2 - V\right) dt\right], \quad (5)$$

where m is the mass of atom, $\hbar$ is the reduced Planck constant, and v and V are respectively the velocity and the potential along each trajectory of 1 and 2 [21, 22]. Instead of calculating exact trajectories under V and photon-recoil kicks from laser pulses, we consider trajectories of free particles subject only to photon-recoil kicks but not forces due to V. This is justified by the following two reasons: First, gravity is largely absent in a freely falling frame (a microgravity environment), the motion

of atoms in UHV is like a free particle to the leading order. Second, the chameleon potential under investigation is small, so that its influence on trajectories can be ignored for the first order calculation. With the choice of using free-particle trajectories, two AI paths will overlap at the beginning and at the end, thus $\psi_{\rm separate} = 0$. Similarly, the kinetic energy terms in Eq. (5) in two paths are identical and do not contribute to $\psi_{\rm prop}$. Finally, $\psi_{\rm laser}$ is under operators' control and will cancel between AIs if a differential measurement scheme is adapted [23, 24], and will be omitted hereafter.

As a result, ψ is simplified to

$$\psi = \psi_{\rm prop} = \frac{1}{\hbar}\left(\int_2 V dt - \int_1 V dt\right) \tag{6}$$

in our first order AI phase calculation. The AI phase due to a chameleon field profile ϕ in the freely falling frame is then obtained by plugging in the chameleon interaction potential $V_{\rm int}$ for a point particle of mass m,

$$\begin{aligned}\psi &= \frac{m}{\hbar}\frac{\beta}{M_{\rm Pl}}\left(\int_2 \phi\ dt - \int_1 \phi\ dt\right) \\ &\simeq 51\beta\left(\int_2 \phi\ dt - \int_1 \phi\ dt\right) \text{mrad},\end{aligned} \tag{7}$$

where m is evaluated for ^{87}Rb, and ϕ is in units of eV.

In the following sections, we will discuss systematics versus chameleon signals in realistic settings based on Eqs. (6) and (7), respectively. The experimental scenarios are assumed in microgravity for all the following discussions, as it is necessary for the concept. It will become clear that only a microgravity environment can support long AI interrogation time for needed high acceleration sensitivity, confined AI trajectories for short-ranged chameleon forces, and feasible systematics control.

V. CONFIGURATION I: SPHERICAL SHELLS

We first consider the case of a spherical shell as it is one of the obvious choices for isolating the chameleon force from the gravitational force. The gravitational force from a uniform shell is zero inside the spherical void while the chameleon force does not vanish, thus ideally no precise knowledge of the shell mass or geometry is needed for a chameleon force measurement. It is also a simple geometry that can be solved by different numerical approaches, and thus allowing comparison of calculation results and validation of scripts for further investigations.

A. The chameleon field

We solve for ϕ in both 1D and 2D settings by utilizing the spherical and the cylindrical symmetry of a spherical shell, respectively. On the one hand, 1D calculation is sufficient for the investigation of using spherical shells, and is faster than higher dimensional calculations. On the other hand, 2D and even 3D solvers are needed when considering realistic vacuum chambers or general material boundaries. Therefore, we develop a stable 1D solver, and compare the result with that published in Ref. [7] to validate the code. 2D and 3D solvers are then developed and checked against the 1D solver for spherical shells.

In the 1D case where only the radial coordinate is relevant, Eq. (2) is in fact an ordinary differential equation instead of a partial differential equation. To calculate $\phi(r)$ in a spherical shell of radius R, $\rho(r)$ is defined as a step function

$$\begin{aligned}\rho(r < R) &= \rho_{\rm vacuum}, \text{ and} \\ \rho(r \geq R) &= \rho_{\rm wall},\end{aligned}$$

on an evenly spaced grid of $\sim$ 5000 points, and the boundary conditions are

$$\begin{aligned}\frac{d\phi}{dr}(0) &= 0, \text{ and} \\ \phi(R + \delta R) &= \phi_{\rm eq}(\rho_{\rm wall}),\end{aligned} \tag{8}$$

where $\phi_{\rm eq}$ is defined in Eq. (4) and $\delta R \sim 0.1R$. As described in Section III, an iterative calculation using the constant initial guess $\phi = \phi_{\rm eq}(\rho_{\rm wall})$ gives a stable solution after few runs. We observe no difference in solution for $\delta R = 0.02R$ to R, a numerical demonstration of the screening effect.

Our result is in good agreement with Ref. [7] for $(n, \Lambda, \beta) = (1, 0.1\text{ meV}, 10^3)$, $R = 5$ cm, and same vacuum and wall densities, where a completely different numerical method was used. Figure 2 shows ϕ calculated for two parameter sets at different R. Note that ϕ increases with R but at a decreasing rate, which suggests that there is a trade-off between the volume of apparatus and the signal size. We choose $R = 10$ cm as a practically realizable geometry for further AI phase estimate and systematics investigation.

B. Dual atom interferometers

In practical experiments, vibration control is a challenge that every sensitive AI measurement has to address, with which the laser phase $\psi_{\rm laser}$ is scrambled by minute displacements of optics, resulting in smeared AI fringes. Differential measurements between simultaneous AIs driven by the same laser pulses have shown great common mode rejection to suppress the influence of vibrations [23, 24]. In addition, differential measurements also suppress some of other systematics including the AC Stark shifts, Zeeman shifts, and wavefront curvatures [15]. Thus, we consider dual AI configurations for the chameleon force detection as shown in Fig. 3.

Two AI configurations are illustrated in Fig. 3, one is the Ramsey-Bordé configuration (bold) and the other is the Mach-Zehnder configuration (dashed). From Eq. (7), the AI phase of the chameleon field will be maximized within a confined region if the two arms stay at different

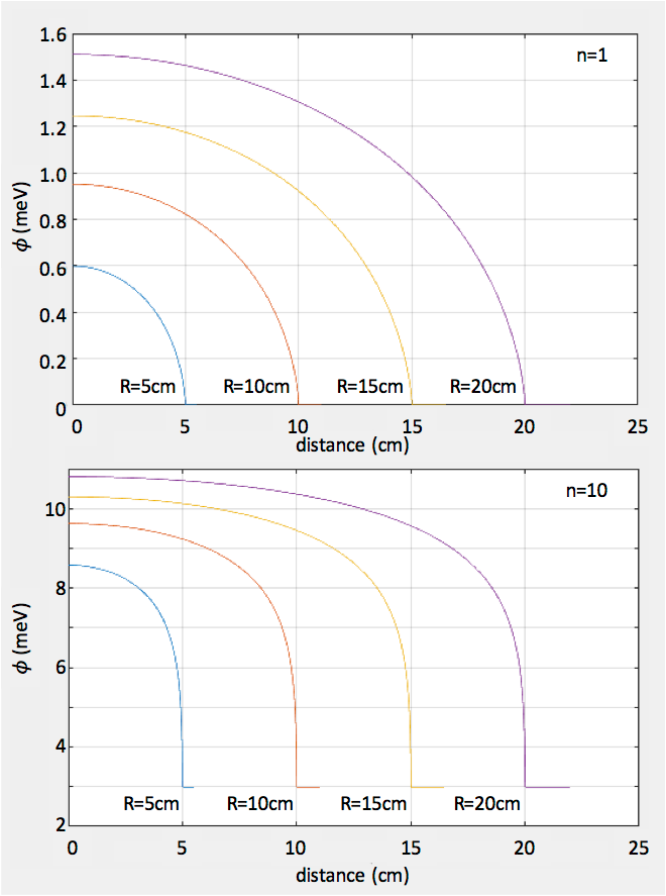

FIG. 2. Chameleon fields inside spherical shells of different radii R as a function of distance to the center of the shell. Upper figure: $(n, \Lambda, \beta) = (1, 0.1 \text{ meV}, 10^3)$. Lower figure: The embracive set $(n, \Lambda, \beta) = (10, 2.4 \text{ meV}, 1)$.

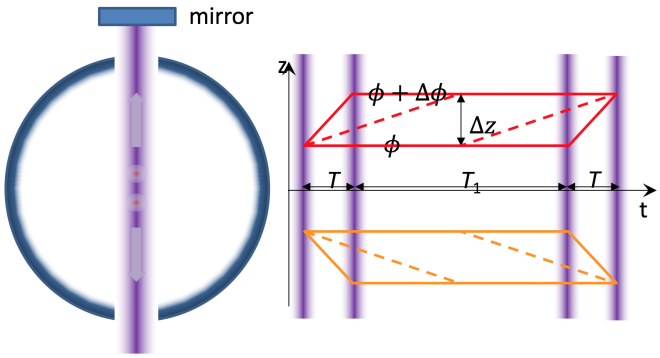

FIG. 3. Depiction of dual AIs in a spherical shell. Left: Two AIs moving from the center towards the sides driven by the same retroreflected laser pulses. Right: Space-time diagram of two AIs. In the Ramsey-Bordé configuration (bold) four $\pi/2$ pulses are applied with separation time T, T_1, and T, while in the Mach-Zehnder configuration (dashed) a $\pi/2$-π-$\pi/2$ pulse sequence is applied with $T_1 = 0$.

potential values for as long as possible, which obviously favors the Ramsey-Bordé configuration with a gain of at most a factor of 2. Note that using large-momentum transfer beamsplitters in the AIs [25] does not increase ψ proportionally, which is generally true for AIs with limited traverse distance. Nevertheless, following Eq. (7), one can easily find that, $\psi = 51\beta \left(\frac{\Delta\phi}{\text{eV}}\right)(T + T_1)\text{mrad}$ in both configurations, where $\Delta\phi$ is the potential difference of ϕ at distance Δz away from the center. Let the $\Delta z =$ 9 cm so that the atomic clouds are not too close to the shell, then $\Delta\phi \simeq 2$ meV for $(n, \Lambda, \beta) = (10, 2.4 \text{ meV}, 1)$, as shown on the $R = 10$ cm curve of the lower plot of Fig. 2. The differential chameleon phase between AIs in Fig. 3 is then $2\psi \simeq 0.2$ mrad for $T + T_1 = 1$ s, which is comfortably accessible with current AI technology.

Equation (7) suggests that one arm of the AI should be kept close to a surface for a long time to increase the sensitivity to $\Delta\phi$, which can be best achieved in microgravity environments. Free-fall of atoms in terrestrial experiments limits the time of close proximity to few ms, and disallows the symmetric arrangement depicted in Fig. 3 for common mode rejections. On the other hand, it is much more feasible to implement AIs of long interrogation time $T + T_1 > 1$ s at a fixed distance $\simeq 1$ cm to surfaces in microgravity, such as in space or drop tower facilities.

Even though there is no gravity force from an ideal shell, the gravity gradients of Earth will contribute significantly to this dual-AI configuration for all near Earth environments including experiments on low Earth orbits such as the International Space Station (ISS), where the Earth's gravity gradient $\gamma_\oplus \simeq 2400/\text{s}^2$. The corresponding differential AI phase, according to Eq. (6), is $2\psi = \frac{m}{\hbar}\gamma_\oplus \Delta z^2 (T + T_1) \simeq 27$ rad. Thus, a suppression factor of $> 10^5$ is required to discern the chameleon signal. Although there exists an AI configuration that can suppress gravity gradients [26], it unsurprisingly reduces the sensitivity to the chameleon field. More significantly, gravity gradients due to nearby masses will not be as uniform as $\gamma_\oplus$, and sufficient knowledge of the mass distribution around the apparatus will again be required, even with the AI technique of using a different photon recoil in the π-pulse to cancel the gravity gradient effect while maintaining the force sensitivity [27, 28]. The sensitivity to ambient gravity gradients also precludes the utilization of drop towers for an implementation of the proposed scheme, in addition to the lack of needed averaging time. A deep space mission, on the other hand, may have a low self gravity gradient satellite operating in a low gravity gradient region, and thus enables a decisive measurement of chameleon theory using spherical shells.

VI. CONFIGURATION II: PERIODIC CHAMELEON FIELD

Despite the simplicity of the geometry and the absence of the gravity interference from the test mass to the chameleon force detection, the spherical shell configuration discussed in the previous Section has practical issues other than manufacturing imperfection that will impact the measurement. In practice, the shell cannot be perfectly spherical with windows and vacuum parts, not to mention other nearby masses including the Earth field gradient if the experiment is performed on or near Earth as discussed before.

Recognizing the fact that the chameleon force field under measurements results from the presence of nearby walls, here we study a mass-wall configuration that creates a chameleon force field of known periodicity while reducing the gravity force and force gradient signal below the expected chameleon forces. In this Section, we will describe 1) simulation of chameleon field with periodic mass structure, 2) multi-loop AI for the periodic signal detection, 3) refined mass wall structure to reduce the gravity force to a minimum, below all expected chameleon force magnitude, and finally 4) a resonance detection scheme with high systematic discrimination.

A. Periodic chameleon field

We consider the chameleon field inside a cylindrical symmetric metal structure within a larger UHV chamber. The structure is constituted of a tube with a number of evenly distributed thin dividers across the symmetry axis and a center bore through all dividers, depicted in Fig. 4a as an example. The corresponding chameleon field for $(n, \Lambda, \beta) = (1, 0.1\text{ meV}, 10^3)$ is shown in Fig. 4b by solving the 2D PDE as described in Section III, with end caps on both ends of the tube. The field will be probed by atoms traversing through the center bore, and the expected chameleon acceleration is plotted in Fig. 4c (according to Eq. (3)), if the chameleon theory is valid and the parameters used in calculating ϕ correspond to reality. Clearly there is periodic acceleration modulation from the chameleon field. The magnitude of the acceleration modulation a_p is ~ 1 nm/s^2 for the parameters used. We notice that, for a given chameleon parameter set, a_p does not depend strongly on the inner radius of the tube or the spacing between dividers, and is more sensitive to the bore diameter. This observation agrees with the physical picture that the chameleon force is short-ranged so that boundary variations farther away have much less impact than variations nearby. The acceleration is much weaker for the embracive parameters $(n, \Lambda, \beta) = (10, 2.4\text{ meV}, 1)$, ~ 5 pm/s^2 as shown in Fig. 5, where off-axis (2.5 mm) axial acceleration is also plotted, showing that the lateral extent of the chameleon force is large enough for a practical AI to probe.

As in all modulation measurement schemes, periodic

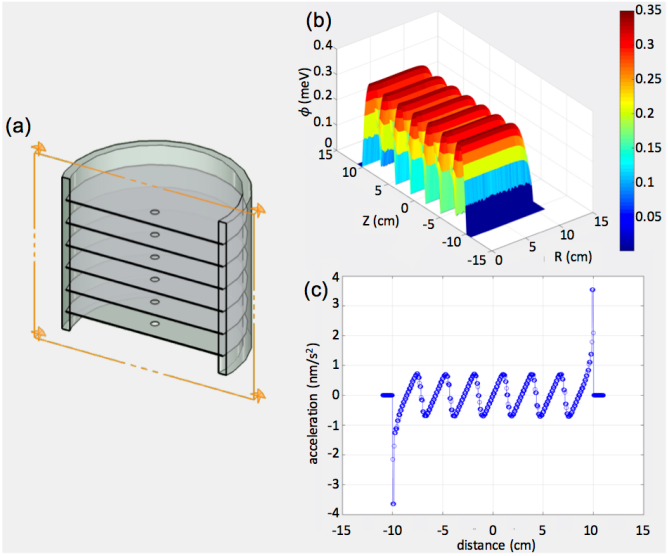

FIG. 4. A periodic structure and the corresponding chameleon field. (a) Depiction of a tube with six dividers and a center bore. (b) The profile of the chameleon field inside a structure with the following dimensions: tube length of 20 cm, tube inner radius of 10 cm, center bore diameter of 1 cm, and divider thickness of 1 mm. The chameleon field is for parameters $(n, \Lambda, \beta) = (1, 0.1\text{ meV}, 10^3)$. Note that additional end caps at the top and the bottom of the tube are assumed in the calculation. (c) Chameleon acceleration on the atoms along the symmetry axis.

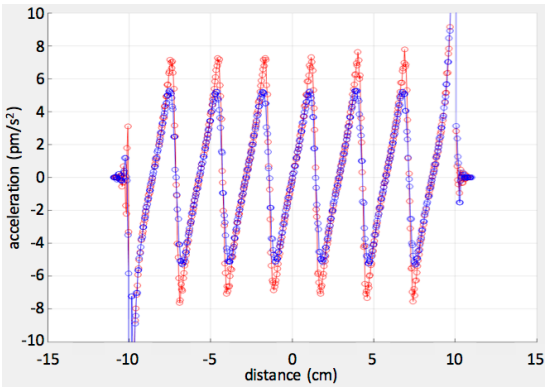

FIG. 5. Axial acceleration for the embracive chameleon parameters $(n, \Lambda, \beta) = (10, 2.4\text{ meV}, 1)$. Blue: axial acceleration on the symmetry axis. Red: axial acceleration 2.5 mm away from the symmetry axis.

signatures can be well separated from systematics of different periodicity, even if the systematics are orders of magnitude larger than the signal size. Figures 4 and 5 show that chameleon fields can exert forces at specific periodicity on test atoms, while gravitational forces from the environment (including Earth) are slowly varying. We anticipate that the gravity gradients of the Earth, the most significant systematic as discussed in Section V B, in differential AI chameleon force detections will be greatly suppressed by using atom interferometers that are only

sensitive to periodic forces.

B. Multi-loop atom interferometers

The periodic force field can be best detected by an AI where the accrued AI phase (Eq. (6)) is modulated in sync with the direction reversal of the force field. A multi-loop AI with two arms crossing each other several times by additional mirror pulses (as shown in Fig. 6) will serve the purpose. Multi-loop AI configurations have been proposed to suppress systematic effects, such as gravity gradients and rotations [19, 26, 29]. Here we use a multi-loop AI configuration to accumulate the dark energy-induced periodic phase change while cancelling other systematics. Again, the perturbative approach justified in Section IV will be adapted to illustrate the concept.

An N-loop AI configuration hereafter is defined as follows. Consider an AI driven by two-photon beamsplitter ($\pi/2$-) and mirror (π-) pulses with atoms initially at rest, as depicted in Fig. 6. After initial $\pi/2$-pulse splitting at $t = 0$, one arm moves away at two photon recoil velocity $2v_r$ (red in Fig. 6) while the other arm remains at rest (blue in Fig. 6). At $t = T$, a π-pulse is applied so that two arms interchange velocity and approach each other. At $t = 2T$, the two arms overlap and the first loop is formed. Instead of applying a $\pi/2$-pulse at $t = 2T$, as in the Mach-Zehnder configuration, no pulse is applied and the two arms proceed across each other initiating the second loop. At $t = 3T$, a π-pulse is applied to bring the two arms closer as the beginning of the second half of the second loop. The pattern continues in that a π-pulse is applied at $t = (2i-1)T$ for $i = 1, 2, \cdots$ until $i = N$, and a $\pi/2$-pulse is applied to close the interferometer at $t = 2NT$. To suppress vibrational noise and other systematics (see Section IV), dual AIs of the same periodicity with precisely controlled separation are desired. This is easily achieved by adding a $\pi/2$-pulse at time T_d before the AI starts, as shown in Fig. 6. The spatial separation of the AIs, δd, is determined solely by the recoil velocity and timing, $\delta d = 2v_r T_d$. Note that the dual N-loop AI scheme can be extended to AIs using large-momentum transfer beamsplitters with photon recoil kick of $2n_b v_r$ per pulse [25] or using atom sources with nonzero initial velocity v_0.

The response of an N-loop AI to a periodic potential is calculated as follows. Consider a 1D sinusoidal potential $V(x)$ of periodicity $1/K$, $V(x) = V_0 \cos(2\pi K(x+d))$, the corresponding acceleration $a(x)$ on a test particle of mass m is

$$\begin{aligned} a(x) &= \frac{V_0}{2\pi K m} \sin(2\pi K(x+d)) \\ &\equiv a_p \sin(2\pi K(x+d)). \end{aligned} \tag{9}$$

The AI phase can be calculated using Eq. (6), which is a function of the number of loops N, the initial position of the atom relative to the potential d, the periodicity $1/K$,

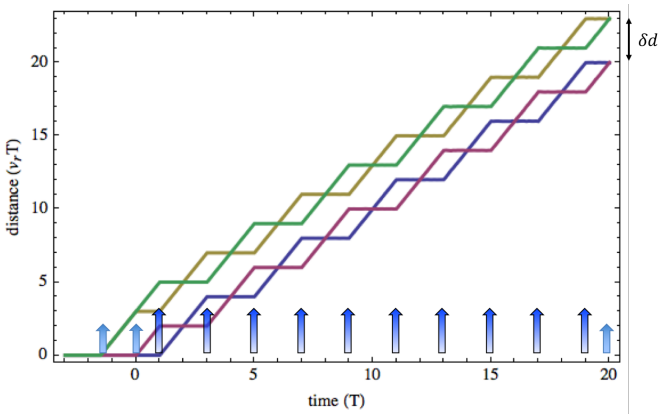

FIG. 6. Space-time diagram of dual 10-loop AIs using two-photon beamsplitters ($n_b = 1$). Arrows on the plot indicate AI pulses at various times, with longer and shorter arrows representing π-pulses and $\pi/2$-pulses, respectively. Lower traces (blue and red) form a 10-loop AI, while upper traces (green and yellow) form another 10-loop AI. Two AIs are derived from a single source by a $\pi/2$-pulse applied in advance of the AI start time ($t = 0$).

the size of beamsplitter photon recoil $n_b v_r$, the pulse separation time T, the initial velocity of the atoms v_0, and the peak acceleration a_p. For example, the phase of the first AI loop is

$$\begin{aligned} \psi_1(d) = &\frac{2n_b k}{(2\pi K)^2 v_0(v_0 + 2n_b v_r)} a_p \\ &\times \Big[-\sin(2\pi K d) + \sin(2\pi K(d + v_0 T)) \\ &+ \sin(2\pi K(d + (v_0 + 2n_b v_r)T)) \\ &- \sin(2\pi K(d + 2(v_0 + n_b v_r)T)) \Big]. \end{aligned} \tag{10}$$

The phase of the second loop is simply

$$\psi_2 = -\psi_1\Big(d + 2(v_0 + n_b v_r)T\Big), \tag{11}$$

due to the change of the starting position after the first loop and the interchange of the trajectories. Thus, the total phase of an N-loop AI is

$$\psi = \sum_{n=1}^{N} -(-1)^n \psi_1\Big(d + 2(n-1)(v_0 + n_b v_r)T\Big). \tag{12}$$

There is no concise general expression for ψ, even in our perturbative approach where free particle trajectories are used. However, it is anticipated that when the periodicity of the potential is synchronized with the loops of the AI, the phase difference of every loop between the two arms will be the same such that the AI phase is linearly proportional to N. In fact, two adjacent loops have phases of opposite signs, due to the position interchange of the arms relative to the potential (Fig. 6). So the periodicity of the AI is determined by the spatial extent of two loops, $4(v_0 + n_b v_r)T$. On the other hand, for asynchronous potentials, the loop phase difference will

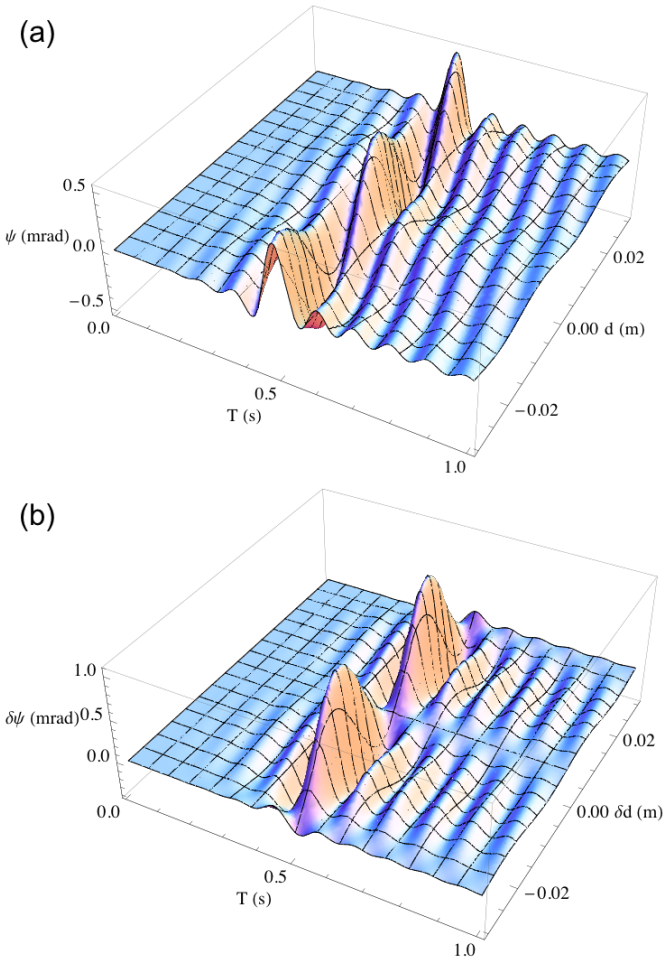

FIG. 7. AI phases of 10-loop AIs. (a) Phase ψ of a 10-loop AI as a function of T and d. (b) Differential phase $\delta\psi$ between dual 10-loop AIs as a function of T and δd, assuming one starts at $d = 0$.

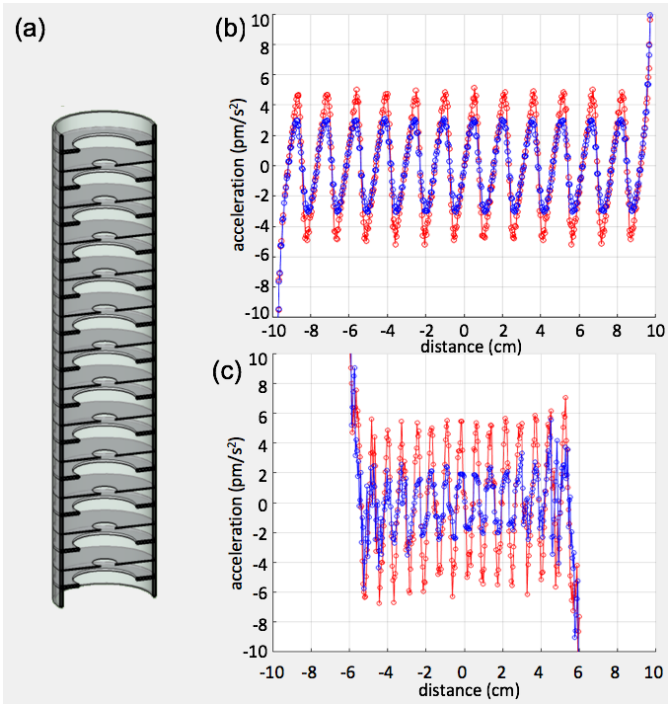

FIG. 8. A periodic structure with 12 dividers and trim masses, and the corresponding gravity and chameleon accelerations. (a) Sketch of the structure. The dimensions are: Tube length 20 cm, radius 1 cm, thickness 1 mm, center bore diameter 1 cm, divider thickness 0.1 mm, trim ring thickness 0.962 mm (1/16 of the divider spacing) radially extended by 8.8 mm from the tube body. The material density is $\rho_{\rm wall}$ =2.7 g/cm^3 (aluminium) rather than 7 g/cm^3 (steel) in previous calculations. (b) The axial chameleon accelerations for the embracive parameters. Shown in red are accelerations 2.5 mm away from the symmetry axis. The calculation is performed with end caps. (c) The axial gravitational acceleration. Additional trim blocks are added on both ends to null the gravity gradient at the middle of the tube, for better visualization of the acceleration modulation. Shown in red are accelerations 2.5 mm away from the symmetry axis. Note that the gravitational acceleration is smaller in amplitude and has different periodicity from the chameleon acceleration.

be different for different loops and eventually cancels out for large N. Note that the insensitivity of multi-loop AIs to influences such as gravity, gravity gradients, and rotations make the free-particle trajectory approximation adapted in Section IV more accurate due to the cancellation of their effects between loops.

As an example, Fig. 7a shows the phase of a 10-loop AI with $v_0 = 2v_r$, $n_b = 2$, $1/K = 0.2/7$ m (same periodicity as in Fig. 4), and $a_p = 10$ pm/s^2. The differential phase $\delta\psi$ between two 10-loop AIs of separation δd can be readily calculated, as shown in Fig. 7b, where one AI starts at $d = 0$. Note that $\delta\psi \simeq 1$ mrad is for a_p about twice of the peak acceleration for the embracive parameters (shown in Fig. 5) with the total AI time $20T \simeq 10$ s at the resonance, which means that an AI with 50% contrast and 10^6 atoms can detect the signal in less than 100 shots!

Moreover, we find that $\delta\psi = 0$ for a constant gravity gradient for even N.

C. Self-gravity force suppression

Despite the insensitivity to constant gravity gradients and ambient perturbations, the structure itself has gravitational force with exactly the same periodicity as the chameleon force. For the structure considered in the above example (Fig. 4), $a_p \simeq 1$ nm/s^2 from the self gravity. Mass proximity modulation [6–8] cannot be performed easily in this case, where one would want to change the dimensions of the structure for differential effects between the gravity and the chameleon field, and eventually would encounter the problem of mass measurement accuracy.

We exploit the fact that chameleon forces are of much shorter range than gravity forces, and develop a structure with trim masses to change the periodicity of the grav-

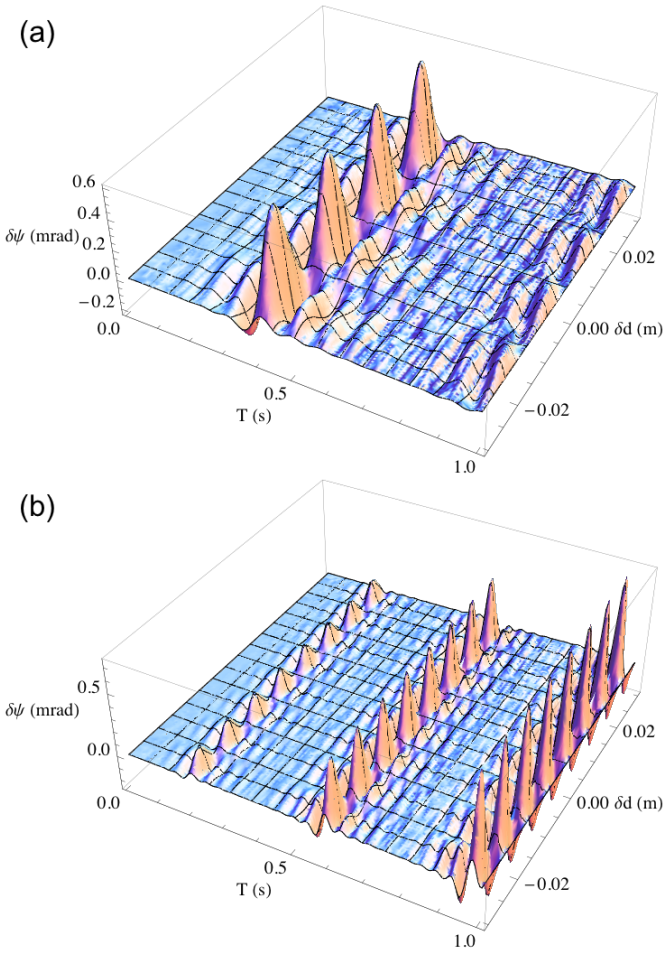

FIG. 9. Differential phase between dual 10-loop AIs as a function of T and δd, with one AI starting at $d = 0$. Both plots assume $a_p = 10$ pm/s^2, $v_0 = 0$, and $n_b = 2$. (a) $1/K = 0.2/13$ m, corresponding to the periodicity of the chameleon acceleration shown in Fig. 8b. (b) $1/K = 0.2/26$ m, corresponding to the periodicity of the gravitational acceleration shown in Fig. 8c.

ity forces, as depicted in Fig. 8a. There are 12 evenly spaced dividers to support 10-loop AIs, and trim rings in between dividers to suppress gravitational forces. Lighter metal of density $\rho_{\rm wall}$ =2.7 g/cm^3 (aluminium) is chosen to reduce the overall self-gravity magnitude. Figure 8b shows the resulting chameleon acceleration for the embracive parameters $(n, \Lambda, \beta) = (10, 2.4 \text{ meV}, 1)$, with a slightly reduced a_p of about 2.6 pm/s^2 compared to Fig. 5. The resulting gravitational acceleration, Fig. 8c, is suppressed below the chameleon acceleration and at twice the spatial frequency. This period-doubled acceleration can be discerned clearly with dual 10-loop AIs, as shown in Fig. 9.

The cancellation of self-gravity forces discussed above relies on the trim masses. We explore the sensitivity to the accuracy of dimensions numerically. Note that the accuracy of the periodicity is not critical, which would only result in slight shift of resonance location in T (Fig. 9). Since the structure is made of single material and the measurement is sensitive to a specific spatial frequency, imperfections such as density inaccuracy, impurity, and inhomogeneity of the material are not of concern to the first order. We evaluate the influence of non-periodic disturbances by simulating the extreme case: one trim ring is completely missing. Depending on the position of the missing ring, the largest projection of the resulting acceleration on the specific spatial frequency has an amplitude of $a_p = 2.5$ pm/s^2. This seemingly sizeable contribution, however, does not exhibit the resonant feature shown in Fig. 9 when T is varied, which allows a clean separation and rejection from the anticipated periodic signal. Clearly, this ability is only possible in a microgravity environment where atomic motions are controlled slow and linear moving states.

The residual periodic inhomogeneity is to be combined with the trim mass dimension inaccuracy analysis as follows. We simulate individually the divider thickness error and three types of trim mass dimension error: the radial extent, the thickness, and the offset from the center of dividers. Plots similar to Fig. 8c are generated for different dimensions, and the peak value of on-axis periodic gravitational acceleration a_p of each simulation is extracted. We find that $a_p < 2$ pm/s^2 for divider thickness changes of $\pm 10\%$ from the design value of 0.1 mm, for trim mass radial extent between 8.4 mm to 9.0 mm, for trim mass thickness changes of $\pm 10\%$ from the design value of 0.962 mm, or for trim mass offset of ± 0.3 mm. These dimension tolerances can be met easily. Variations among trim mass rings or dividers have less impact than common errors considered in the analysis and are ignored, since they will contribute less in magnitude and at wrong periodicity.

D. Resonant detection and systematic suppression

The main motivation of using the periodic structure is to reduce the uncontrollable systematics while increasing the intended signal. While the signal accumulates with the multi-loop AI for the periodic field, the real power lies in the ability to show the measurement sensitivity to the periodicity with the experimentally controllable parameters, here we call it resonance detection.

Figure 9a shows the anticipated differential AI phase for the chameleon acceleration (Fig. 8b) as a function of T and the separation δd between two 10-loop AIs. Similar periodic feature can be obtained by varying the starting location of the dual AIs (the d parameter in Fig. 7a). As expected from a modulation detection scheme, the signal is strongest when the modulation is in sync with the periodicity of the signal and is greatly suppressed otherwise. The capability of scanning T and δd, e.g., around $T = 0.5, \delta d = 0.01$ in Fig. 9a, allows an unambiguous detection of the chameleon signal, even without precise knowledge or tight tolerance of the mechanical structure. For signals out of sync with the multi-loop AIs, such as

the residual gravity forces shown in Fig. 8c, their contribution in the region around $T = 0.5, \delta d = 0.01$ is small with different signature. Likewise, the blackbody radiation effect due to temperature gradients [30] is also nonresonant with the structure and therefore suppressed. As a result, the multi-loop AIs proposed in Section VI B not only have sensitivity for the weakest chameleon forces, but also segregate gravity forces from the wall, the mass of nearby apparatus, and the Earth. This enables a complete chameleon theory validation experiment in a near Earth microgravity environment.

The insensitivity to gravity and gravity gradients also provides an important technical advantage that strongly enhances the feasibility of the multi-loop AIs. Gravity gradients have been a major and difficult systematic effect for precision measurements [20]. Due to the initial position sensitivity of AI in the Mach-Zehnder configuration and the finite extent of atomic clouds, fringes in the clouds are anticipated for long T interferometers, which result in lost of contrast and require additional efforts to recover the AI phase (as discussed in Ref. [15] for example). On the contrary, each multi-loop AI discussed above has zero sensitivity to gravity, and the sensitivity to gravity gradient as γNT^3 rather than $\gamma(NT)^3$, so that the AI phase is significantly less sensitive to the initial position and velocity in the presence of gravity and gravity gradients compared to that of a Mach-Zehnder AI of the same duration. Thus, the contrast of a multi-loop AI does not suffer greatly from gravity gradient induced smearing. Similarly, rotation-induced fringes and contrast loss are also suppressed in multi-loop AIs. A straightforward implementation of multi-loop AIs should have high contrast even for long T without modification of the AI sequence or imaging of the clouds. It can be shown that adapting the gravity gradient cancellation method described in Refs. [27, 28] will further remove the residual sensitive without reducing the chameleon signal size. In contrast to the spherical shell configuration considered in Section V, measurements in this periodic structure configuration is insensitive to ambient gravity gradients, which allows an implementation in drop tower facilities.

To put the numbers into perspective, the differential AI phase $\delta\psi \simeq 0.12$ mrad for the triangular acceleration pattern of $a_p = 3$ pm/s^2 (inferred from Fig. 9a and Fig. 8b respectively). The phase resolution of $\delta\psi$ is 4 mrad per shot for dual AIs, each of which has 10^6 atoms, 50% fringe contrast, and random common phase. Phase resolution of 0.12 mrad can thus be reached within 1200 shots, which is less than 7 hours assuming a duty cycle of 20 s. Suppose 10 measurement sets are desired to explore the resonance feature in T and δd (Fig. 9a), the chameleon theory can be invalidated with high fidelity in 3 days of continuous operation of such an experiment onboard the ISS. Even with very conservative parameters of 10^5 atoms each and 10% contrast, a conclusive result will be obtained in 25 months of operation. The atom source and AI requirements are well within the capability of the Cold Atom Laboratory (CAL) to be deployed on the ISS in 2018 [31], while cold atom technologies have been demonstrated in microgravity in projects such as Ref. [18]. In principle, it is also feasible to conduct such experiment in a drop tower such the Einstein Elevator [32] where sufficient averaging time can be accumulated with high drop rate.

VII. CONCLUSIONS

The chameleon scalar field theory is a promising candidate of dark energy. Atom interferometers bypass its screening effect that prevents laboratory detection using bulk materials. We present a numerical method to efficiently calculate chameleon fields near material surfaces of nontrivial geometry, and develop measurement schemes using atom interferometry that suppress major systematic effects. Specifically, a multi-loop atom interferometer configuration is designed to resonantly detect the periodic chameleon forces and suppress gravitational effects from self-mass and its environment. For this scheme to work, the experiment can only be carried out in a microgravity reference frame where atoms are slow and linear. The simulations and analyses show that such an experiment can be readily implemented in an apparatus similar to CAL in the ISS platform and will help provide answers to the mystery of dark energy.

ACKNOWLEDGMENTS

The authors would like to acknowledge valuable discussions with Jason Rhodes, Olivier Doré, Phil Bull, Jérôme Gleyzes, and Holger Müller. This work was carried out at the Jet Propulsion Laboratory, California Institute of Technology, under a contract with the National Aeronautics and Space Administration.

[1] Edmund J. Copeland, M. Sami, and Shinji Tsujikawa. Dynamics of dark energy. *International Journal of Modern Physics D*, 15(11):1753–1935, 2006.

[2] Austin Joyce, Bhuvnesh Jain, Justin Khoury, and Mark Trodden. Beyond the cosmological standard model. *Physics Reports*, 568:1 – 98, 2015. Beyond the cosmological standard model.

[3] Jeremy Sakstein. Tests of gravity with future space-based experiments. *arXiv preprint arXiv:1710.03156*, 2017.

[4] Justin Khoury and Amanda Weltman. Chameleon fields: Awaiting surprises for tests of gravity in space. *Phys. Rev. Lett.*, 93:171104, Oct 2004.

[5] Clare Burrage, Edmund J. Copeland, and E.A. Hinds. Probing dark energy with atom interferometry. *Journal*

of Cosmology and Astroparticle Physics, 2015(03):042, 2015.

[6] P. Hamilton, M. Jaffe, P. Haslinger, Q. Simmons, H. Müller, and J. Khoury. Atom-interferometry constraints on dark energy. *Science*, 349(6250):849–851, 2015.

[7] Benjamin Elder, Justin Khoury, Philipp Haslinger, Matt Jaffe, Holger Müller, and Paul Hamilton. Chameleon dark energy and atom interferometry. *Phys. Rev. D*, 94:044051, Aug 2016.

[8] Matt Jaffe, Philipp Haslinger, Victoria Xu, Paul Hamilton, Amol Upadhye, Benjamin Elder, Justin Khoury, and Holger Müller. Testing sub-gravitational forces on atoms from a miniature in-vacuum source mass. *Nature Physics*, 13(10):938–942, 2017.

[9] Peter J. Mohr, David B. Newell, and Barry N. Taylor. Codata recommended values of the fundamental physical constants: 2014. *Journal of Physical and Chemical Reference Data*, 45(4):043102, 2016.

[10] Amol Upadhye. Dark energy fifth forces in torsion pendulum experiments. *Physical Review D*, 86(10):102003, 2012.

[11] Paul R Berman and Vasili Kharchenko. Atom interferometry, 1997.

[12] Alexander D. Cronin, Jörg Schmiedmayer, and David E. Pritchard. Optics and interferometry with atoms and molecules. *Rev. Mod. Phys.*, 81(3):1051–1129, Jul-Sep 2009.

[13] Mark Kasevich and Steven Chu. Atomic interferometry using stimulated raman transitions. *Physical review letters*, 67(2):181, 1991.

[14] Jason M Hogan, David MS Johnson, and Mark A Kasevich. Light-pulse atom interferometry. *Rotation of the Earth*, 34:5, 2008.

[15] Jason Williams, Sheng-wey Chiow, Nan Yu, and Holger Müller. Quantum test of the equivalence principle and space-time aboard the international space station. *New Journal of Physics*, 18(2):025018, 2016.

[16] Susannah M Dickerson, Jason M Hogan, Alex Sugarbaker, David M S Johnson, and Mark A Kasevich. Multiaxis inertial sensing with long-time point source atom interferometry. *Phys Rev Lett*, 111(8):083001, Aug 2013.

[17] A Bonnin, N Zahzam, Y Bidel, and A Bresson. Characterization of a simultaneous dual-species atom interferometer for a quantum test of the weak equivalence principle. *Physical Review A*, 92(2):023626, 2015.

[18] Jan Rudolph, Naceur Gaaloul, Yeshpal Singh, Holger Ahlers, Waldemar Herr, Torben A Schulze, Stephan Tobias Seidel, Christina Rode, Vladimir Schkolnik, Wolfgang Ertmer, et al. Degenerate quantum gases in microgravity. *Microgravity Science and Technology*, 23(3):287–292, 2011.

[19] Jason M Hogan, David MS Johnson, Susannah Dickerson, Tim Kovachy, Alex Sugarbaker, Sheng-wey Chiow, Peter W Graham, Mark A Kasevich, Babak Saif, Surjeet Rajendran, et al. An atomic gravitational wave interferometric sensor in low earth orbit (AGIS-LEO). *General Relativity and Gravitation*, 43(7):1953–2009, 2011.

[20] Sheng-wey Chiow, Jason Williams, Nan Yu, and Holger Müller. Gravity-gradient suppression in spaceborne atomic tests of the equivalence principle. *Physical Review A*, 95(2):021603, 2017.

[21] Pippa Storey and Claude Cohen-Tannoudji. The Feynman path integral approach to atomic interferometry. A tutorial. *Journal de Physique II*, 4(11):1999–2027, 1994.

[22] Achim Peters, Keng Yeow Chung, and Steven Chu. High-precision gravity measurements using atom interferometry. *Metrologia*, 38(1):25, 2001.

[23] J. M. McGuirk, G. T. Foster, J. B. Fixler, M. J. Snadden, and M. A. Kasevich. Sensitive absolute-gravity gradiometry using atom interferometry. *Physical Review A*, 65(3):033608, 2002.

[24] Sheng-wey Chiow, Jason Williams, and Nan Yu. Noise reduction in differential phase extraction of dual atom interferometers using an active servo loop. *Physical Review A*, 93(1):013602, 2016.

[25] Holger Müller, Sheng-wey Chiow, and Steven Chu. Atom-wave diffraction between the raman-nath and the bragg regime: Effective rabi frequency, losses, and phase shifts. *Physical review A*, 77(2):023609, 2008.

[26] B Dubetsky and MA Kasevich. Atom interferometer as a selective sensor of rotation or gravity. *Physical Review A*, 74(2):023615, 2006.

[27] Albert Roura. Circumventing heisenberg's uncertainty principle in atom interferometry tests of the equivalence principle. *Physical review letters*, 118(16):160401, 2017.

[28] G D'Amico, G Rosi, S Zhan, L Cacciapuoti, M Fattori, and GM Tino. Canceling the gravity gradient phase shift in atom interferometry. *Physical review letters*, 119(25):253201, 2017.

[29] Stephan Kleinert, Endre Kajari, Albert Roura, and Wolfgang P. Schleich. Representation-free description of light-pulse atom interferometry including non-inertial effects. *Physics Reports*, 605:1 – 50, 2015.

[30] Philipp Haslinger, Matt Jaffe, Victoria Xu, Osip Schwartz, Matthias Sonnleitner, Monika Ritsch-Marte, Helmut Ritsch, and Holger Müller. Attractive force on atoms due to blackbody radiation. *arXiv preprint arXiv:1704.03577*, 2017.

[31] http://coldatomlab.jpl.nasa.gov.

[32] https://www.hitec.uni-hannover.de/einsteinelevator.html.